Geomagnetic field modeling from satellite attitude control magnetometer measurements

Jeong Woo Kim,[1] Jong Sun Hwang,[2,3] Ralph R. B. von Frese,[4] Hyung Rae Kim,[5] and Seon-Ho Lee[6]

Received 12 September 2005; revised 20 October 2006; accepted 28 November 2006; published 30 May 2007.

[1] To demonstrate the utility of satellite attitude control magnetometer measurements for mapping main field variations, we analyzed the three-axis magnetometer (TAM) measurements that provide attitude control for the KOMPSAT-1 satellite. Initial processing involved transforming the TAM's magnetic measurements from the Earth-Centered Inertial coordinates (ECI) to the Earth-Centered Earth-Fixed coordinates (ECEF) and then to spherical coordinates. The magnetic field of the satellite body produces symmetric signatures in the ascending and descending orbital measurements and thus can be readily removed. Spectral correlation filtering of the orbital observations helped to eliminate the dynamic external field and solar activity noise components. The ascending and descending data were then spectrally reconstructed to estimate the total magnetic field with minimum track line noise. Correlation coefficients of 0.97 and 0.96 mark the correlation of the KOMPSAT-1 total geomagnetic intensity map with the Ørsted and IGRF2000 core magnetic field models, respectively. Power spectra from Gauss coefficients of KOMPSAT-1 model showed closeness with the models from Ørsted data and IGRF2000 model. The spherical harmonic coefficients calculated from the KOMPSAT-1 model by conjugate gradient inversion are strongly coherent with the Ørsted and IGRF2000 coefficients through degree 9.

Citation: Kim, J. W., J. S. Hwang, R. R. B. von Frese, H. R. Kim, and S.-H. Lee (2007), Geomagnetic field modeling from satellite attitude control magnetometer measurements, *J. Geophys. Res.*, *112*, B05105, doi:10.1029/2005JB004042.

1. Introduction

[2] Our understanding of the spatial and secular variations of the Earth's main or core magnetic field is based largely on about a few hundred years of geomagnetic observatory data [e.g., *Campbell*, 1997; *Chapman and Bartels*, 1940; *Langel and Hinze*, 1998]. However, the observatory record is biased to the terrestrial regions of the northern hemisphere, and also spotty in coverage as observatory operations have waxed and waned with changing funding priorities. In 1951, an airborne geomagnetic survey "Project Magnet" was initiated by the U.S. Naval Oceanographic Office. Two aircrafts were employed in the project to gather magnetic data over the ocean areas to map magnetic intensities and variations [*UFO Investigator*, 1963]. Although the Project Magnet filled many ocean gaps, the coverage from the project was rather limited.

[3] To help mitigate these limitations, core field modeling efforts commonly augment observatory data with temporal snapshots of the geomagnetic field from low Earth orbiting (LEO) satellite magnetic mapping missions [e.g., *Langel and Hinze*, 1998].

[4] Satellite magnetic observations provide important constraints on the behavior of the core field at 300 km and higher altitudes where observatories are lacking and over the southern hemisphere where the observatory coverage is quite poor. Modern core field modeling efforts principally incorporate the magnetic measurements from the U.S. POGO and Magsat [*Langel and Hinze*, 1998], and the presently orbiting Danish Ørsted [*Olsen*, 2002] and German CHAMP [*Maus et al.*, 2002] missions. However, these satellite magnetic observations provide only a discontinuous temporal record of geomagnetic field behavior that is limited to the 1964–1974 period of the POGO satellites, the 6-month period starting in November 1979 of Magsat, and the periods since February 1999 for Ørsted and July 2000 for CHAMP, for measurement accuracies of 10 nT or better.

[5] Since the dawn of the satellite era in the late 1950s, however, LEO satellites have carried onboard magnetometers for attitude control. The present study demonstrates the utility of these measurements for extracting effective core field components. Although not as accurate as measure-

[1]Department of Geoinformation Engineering, Sejong University, Seoul, South Korea.
[2]Department of Earth System Sciences, Yonsei University, Seoul, South Korea.
[3]Also at Geohazard Information Laboratory, Sejong University, Seoul, South Korea.
[4]School of Earth Sciences, Ohio State University, Columbus, Ohio, USA.
[5]Goddard Earth Sciences and Technology Center, University of Maryland Baltimore County at Planetary Geodynamics Laboratory, NASA Goddard Space Flight Center, Greenbelt, Maryland, USA.
[6]Satellite Control System Department, Korea Aerospace Research Institute, Daejeon, South Korea.

Copyright 2007 by the American Geophysical Union.
0148-0227/07/2005JB004042$09.00

ments from the conventional geomagnetic satellite missions, the estimates from onboard satellite attitude control magnetometers can provide important constraints on the behavior of the core field over the roughly 31-year period since 1958 when the conventional magnetic missions were not operating and only available observatory observations were used for core field modeling [*Jensen and Cain*, 1962; *Cain*, 1966].

[6] To demonstrate the utility of satellite attitude control magnetometer measurements for mapping main field variations, we analyzed the three-axis magnetometer (TAM) measurements from the Korean Earth observing satellite Korea Multi Purpose Satellite-1 (KOMPSAT-1). This 3-year mission was launched into a 685-km altitude, Sun-synchronous circular polar orbit on 20 December 1999 with an inclination of 98.13°. The 500 kg spacecraft carried an electro-optical camera, ocean-scanning multispectral imager, and a plasma particle sensor (http://kompsat.kari.re.kr).

[7] The KOMPSAT-1 mission did not have the geomagnetic field observing objectives of the Ørsted and CHAMP missions, and thus its TAM lacked the sensitivity of the Ørsted and CHAMP magnetometers. Specifically, the TAM's sensitivity was 100 nT over the dynamic range of 60,000 nT at the sampling rate of 4 Hz, while Ørsted and CHAMP carry fluxgate and Overhauser sensors that have a common sensitivity of 0.5 nT with sampling rates of 100 Hz and 1 Hz, respectively [*Neubert et al.*, 2001]. Thus the poorer accuracy of the TAM precludes efforts to extract effective lithospheric components where anomaly magnitudes range only over several nT at KOMPSAT-1's altitude. However, the TAM data can be effectively evaluated for lower-degree harmonic coefficients of the core field up to the degree and order 10 with reasonable accuracy.

[8] The following sections describe the data processing that included removing obvious measurement errors from the TAM observations. The measurements were then transformed into Earth-centered coordinates and sorted into ascending and descending orbital data sets for additional noise suppression. The data were gridded and processed further to eliminate external field and track line noise. The resultant KOMPSAT-1 total field model was compared with the global IGRF2000 model as well as the Ørsted model for the same period because the satellites have comparable orbital characteristics in inclination and altitude. We then calculate spherical harmonic coefficients for the resulting Z component values up to degree and order 10 using the conjugate gradient method [*Hestenes and Stiefel*, 1952; *William et al.*, 1986] for comparison with the related coefficients from the Ørsted and IGRF 2000 models.

2. Geomagnetic Field Estimates From the TAM of KOMPSAT-1

[9] This study considers 63 orbital tracks of KOMPSAT-1 obtained over 19–21 June 2000. The tracks were grouped into ascending and descending data sets based on their local magnetic times to enhance the perception of external fields in the KOMPSAT-1 maps [*Arkani-Hamed and Strangway*, 1986; *Kim*, 1996; *Alsdorf et al.*, 1994]. The ascending and descending data were processed next into independent maps that were then merged by spectral reconstruction [*Kim et al.*, 1998] to produce a total field magnetic map [*Kim et al.*, 2003]. Below we describe additional details for implementing these procedures.

2.1. Coordinate Transformation

[10] KOMPSAT-1's geomagnetic data were transformed from the body-centered coordinates (X, Y, Z centered on KOMPSAT-1) to the Earth-Centered Inertial (ECI) spherical coordinates according to

$$\mathbf{V}_{\mathrm{BODY}} = T\mathbf{V}_{\mathrm{ECI}} \tag{1}$$

where $\mathbf{V}_{\mathrm{BODY}}$, $\mathbf{V}_{\mathrm{ECI}}$ are the body and ECI coordinate vectors, respectively. The transformation matrix from the body (X, Y, Z) to ECI (X', Y', Z') coordinates [*Siouris*, 1993] is

$$T = \begin{pmatrix} X' \\ Y' \\ Z' \end{pmatrix} = \begin{pmatrix} q_0^2 + q_1^2 - q_2^2 - q_3^2 & 2(q_3q_0 + q_1q_2) & 2(q_1q_3 - q_0q_2) \\ 2(q_1q_2 - q_3q_0) & q_0^2 - q_1^2 + q_2^2 - q_3^2 & 2(q_1q_0 + q_3q_2) \\ 2(q_0q_2 + q_1q_3) & 2(q_2q_3 - q_0q_1) & q_0^2 - q_1^2 - q_2^2 + q_3^2 \end{pmatrix} \begin{pmatrix} X \\ Y \\ Z \end{pmatrix}, \tag{2}$$

where q_0, q_1, q_2, q_3 are Quaternion estimates of body positions obtained from the KOMPSAT-1 data. The ECI coordinate system is typically defined as a Cartesian coordinate system, where the coordinates are defined as the distance from the origin along the three orthogonal axes. The Z axis runs along the Earth's rotational axis pointing north, the X axis points in the direction of the vernal equinox, and the Y axis completes the right-handed orthogonal system. We then transformed the data from the ECI coordinates to the Earth-Centered Earth-Fixed coordinates (ECEF) coordinates where the Z axis runs along the Earth's rotational axis pointing north, while X and Y axes run along 0° and 90°E, respectively, in the plane of equator [*Chatfield*, 1997; *Kelso*, 1995].

[11] Figure 1 gives the total magnetic field component (F) values from the ascending (A) and descending (B) ground tracks for the 63 orbits after the coordinate transformations were applied. No data poleward of 81.81° N and S were obtained because KOMPSAT-1's inclination was 98.13°. The gridded estimates of the two maps have a correlation coefficient (CC) of 0.73 that translates into the noise level of about 61% using the approximate noise-to-signal (N/S) ratio given by [*Foster and Guinzy*, 1967; *Kim*, 1996]

$$(N/S) \cong \sqrt{\frac{1}{|CC|} - 1}. \tag{3}$$

2.2. Eliminating Satellite and External Magnetic Fields

[12] The KOMPSAT-1's TAM is located inside the satellite bus, and thus its measurements also include the fields due to the electronic components. However, these components produce symmetric signals in the ascending and descending orbital phases that facilitate identifying and removing their effects. The TAM measurements are also affected by external field variations that induce effects from

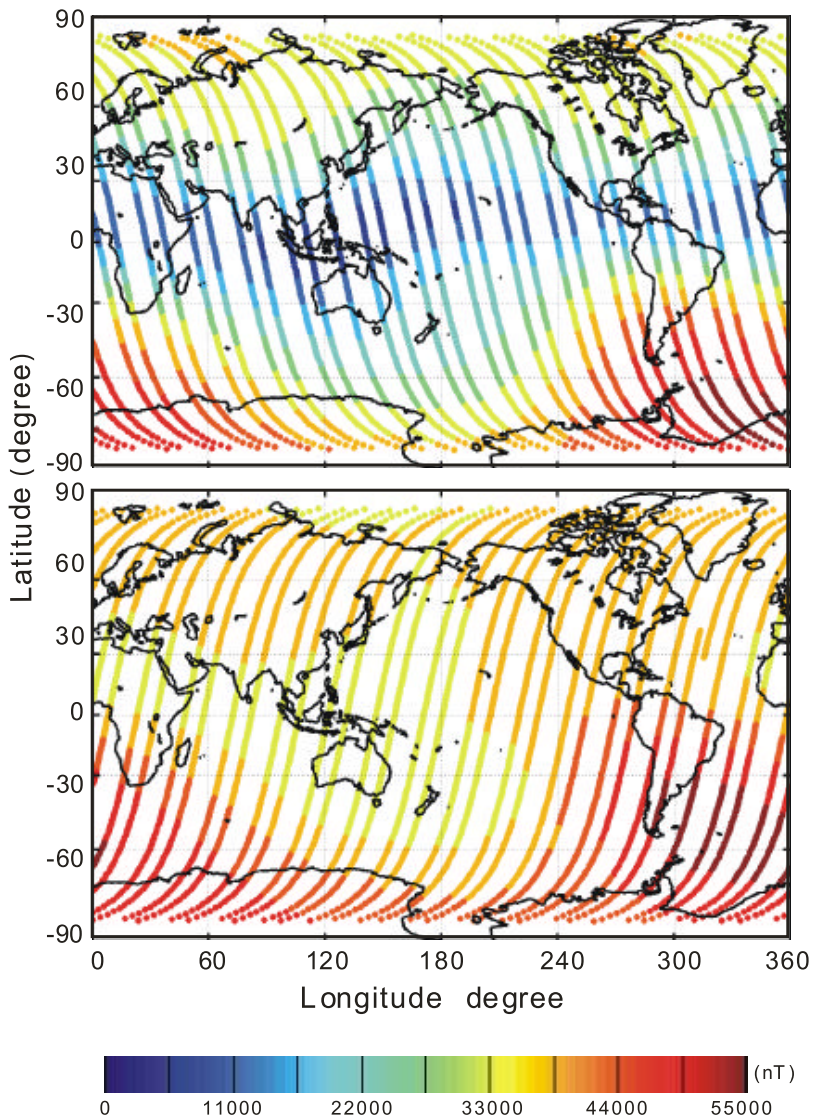

Figure 1. Geomagnetic field measurements from KOMPSAT-1 TAM data acquired from the (top) ascending and (bottom) descending orbits.

the electronic components as well as from any Earth conductors.

[13] Thus the measurement $B_{\mathrm{TAM}}(t)$ from the TAM of KOMPSAT-1 is given by

$$B_{\mathrm{TAM}}(t) = B(t) + B_{\mathrm{BODY}}(t) + B_{\mathrm{SUN}}(t), \tag{4}$$

where $B(t)$is a geomagnetic field measured at the time of t, and $B_{\mathrm{BODY}}(t)$ and $B_{\mathrm{SUN}}(t)$ are induced fields by satellite body itself and the solar effects, respectively. The $B_{\mathrm{SUN}}(t)$ is further given by

$$B_{SUN}(t) = B_{\mathrm{IND-BODY}}(t) + B_{\mathrm{EXT}}(t) + B_{\mathrm{EXT-EARTH}}(t), \tag{5}$$

where $B_{\mathrm{IND\text{-}BODY}}$ is the solar-induced field from the satellite body, B_{EXT} is the external field effect, and $B_{\mathrm{EXT\text{-}EARTH}}$ is the B_{EXT}-induced field from the Earth because the Earth is a conductor. Let T be the period of KOMPSAT-1's revolution, then

$$B_{\mathrm{SUN}}(t) = B_{\mathrm{SUN}}(t + T), \tag{6}$$

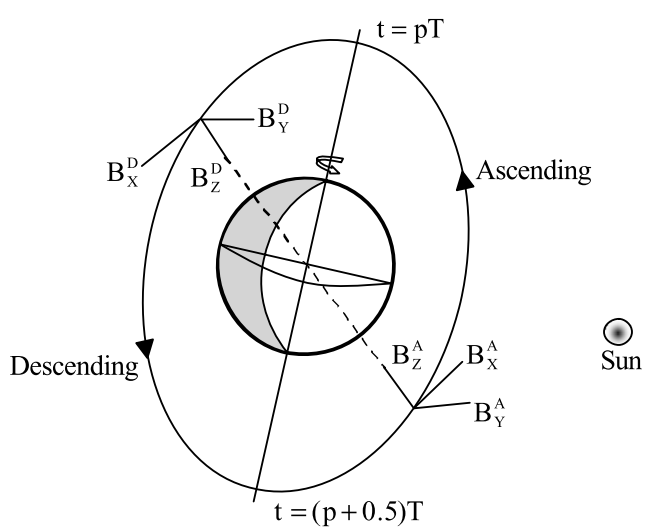

Figure 2. Body coordinates of KOMPSAT-1 body in the ascending and descending modes for elimination of the satellite-induced field component.

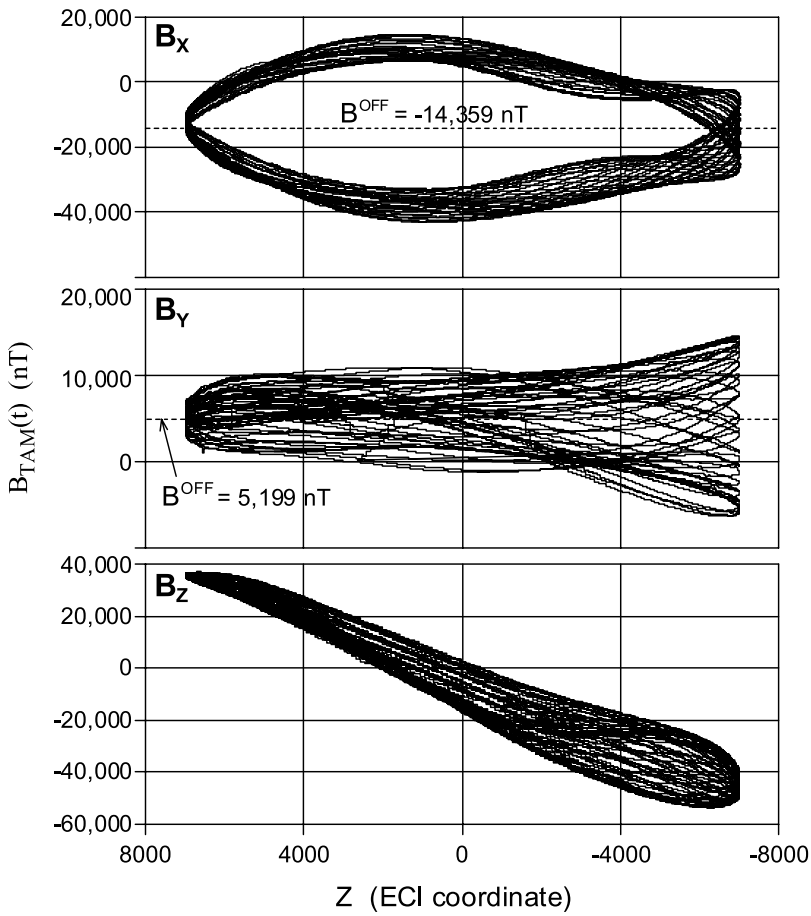

Figure 3. Symmetric nature of the KOMPSAT-1's $B_{\mathrm{TAM}}(t)$ measurements in the ECI coordinate. The X components, (top) B_X^{TAM}, and the Y components, (middle) B_Y^{TAM}, are normally symmetric along the horizontal axes with offset values of $B_X^{\mathrm{OFF}} = -14{,}359$ nT and $B_Y^{\mathrm{OFF}} = 5199$ nT, respectively. (bottom) Z components. B_Z^{TAM} measurements lack symmetry.

assuming that the solar effects are relatively small due to nighttime observations in lower altitude where specially stronger external fields are ineffective.

[14] Assuming that the ψ_p is the magnetic field measured during the pth revolution of the KOMPSAT-1, then

$$\begin{aligned}\psi_p[B_{\mathrm{TAM}}(t)] &\cong \psi_p[B(t)] + \psi_p[B_{\mathrm{BODY}} \\ &\quad + B_{I\mathrm{ND-BODY}} + B_{\mathrm{EXT}} + B_{\mathrm{EXT-EARTH}}] \\ &= \psi_p[B(t)] + B_{\mathrm{XYZ}}^{\mathrm{OFF}},\end{aligned} \tag{7}$$

where $pT \leq t < (p+1)T$, and $B_{\mathrm{XYZ}}^{\mathrm{OFF}}$ are the offset values of B in the X, Y, and Z components. To compensate the $B_{\mathrm{X}}^{\mathrm{OFF}}$ and $B_{\mathrm{Y}}^{\mathrm{OFF}}$ components, we can take advantage of their symmetry in ascending and descending orbital phases because we have a large number ($Np = 63$)of KOMPSAT-1 revolutions [*Lee et al.*, 2001, 2004].

[15] Therefore the X components acquired for the ascending B_X^A and descending B_X^D modes (Figure 2) can be expressed as

$$\sum_{p=1}^{N_p} \int_{pT}^{pT+T/2} \Psi_p\left[B_X^D(\tau)\right] d\tau = -\sum_{p=1}^{N_p} \int_{pT+T/2}^{(p+1)T} \Psi_p\left[B_X^A(\tau)\right] d\tau. \tag{8}$$

Similarly, the Y components acquired for ascending B_Y^A and descending B_Y^D modes are

$$\sum_{p=1}^{N_p} \int_{pT}^{pT+T/2} \Psi_p\left[B_Y^D(\tau)\right] \mathrm{d}\tau = -\sum_{p=1}^{N_p} \int_{pT+T/2}^{(p+1)T} \Psi_{\mathrm{p}}\left[B_Y^A(\tau)\right] \mathrm{d}\tau, \tag{9}$$

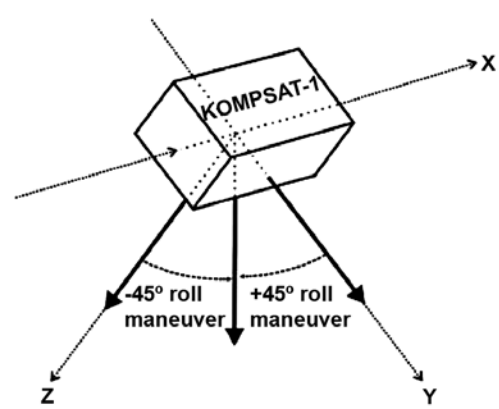

Figure 4. Roll maneuver of KOMPSAT-1 for removing the self-induced magnetic field from the TAM data.

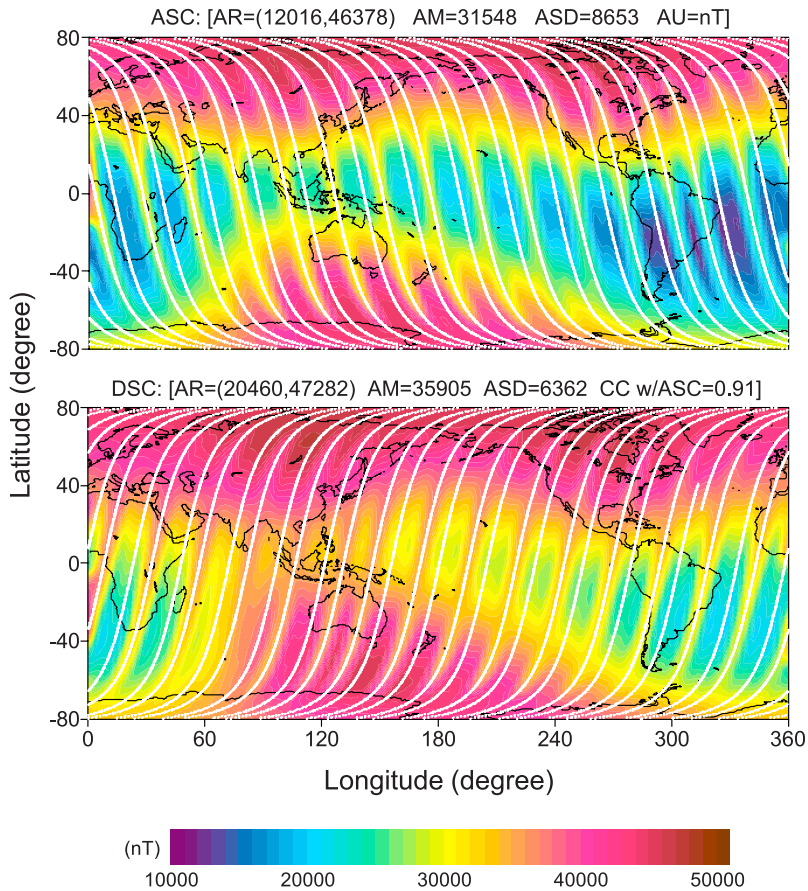

Figure 5. Total geomagnetic field estimates after removing the self-induced field noise from the (top) ascending and (bottom) descending orbits.

where $pT \le t < pT + T/2$. From equations (7), (8), and (9), we get

$$\sum_{p=1}^{N_p} \int_{pT}^{pT+T/2} \left(\Psi_p \left[\left(B_X^{\mathrm{TAM}} \right)^D (\tau) \right] - B_X^{\mathrm{OFF}} \right) \mathrm{d}\tau = -\sum_{p=1}^{N_p} \int_{pT+T/2}^{(p+1)T} \cdot \left(\Psi_p \left[\left(B_X^{\mathrm{TAM}} \right)^A (\tau) \right] - B_X^{\mathrm{OFF}} \right) \mathrm{d}\tau, \quad (10)$$

$$\sum_{p=1}^{N_p} \int_{pT}^{pT+T/2} \left(\Psi_p \left[\left(B_Y^{\mathrm{TAM}} \right)^D (\tau) \right] - B_Y^{\mathrm{OFF}} \right) \mathrm{d}\tau = -\sum_{p=1}^{N_p} \int_{pT+T/2}^{(p+1)T} \cdot \left(\Psi_p \left[\left(B_Y^{\mathrm{TAM}} \right)^A (\tau) \right] - B_Y^{\mathrm{OFF}} \right) \mathrm{d}\tau. \quad (11)$$

Therefore, from equations (10) and (11), we can finally get B_X^{OFF} and B_Y^{OFF}

$$B_X^{\mathrm{OFF}} = \frac{1}{\mathrm{N_P T}} \sum_{p=1}^{N_p} \int_{pT}^{(p+1)T} \Psi_p \left[B_X^{\mathrm{TAM}}(\tau) \right] \mathrm{dt}, \quad (12)$$

$$B_Y^{\mathrm{OFF}} = \frac{1}{\mathrm{N_P T}} \sum_{p=1}^{N_p} \int_{pT}^{(p+1)T} \mathrm{Y_p} \left[B_Y^{\mathrm{TAM}}(\mathrm{t}) \right] \mathrm{dt}. \quad (13)$$

[16] In ECI coordinates, the symmetric properties of the KOMPSAT-1's $B_{\mathrm{TAM}}(t)$, measurements analyzed in this study are shown in Figure 3. The X components, B_X^{TAM} (upper), and the Y components, B_Y^{TAM} (middle), are essentially symmetric along the horizontal Z axes with offset values of $B_X^{\mathrm{OFF}} = -14{,}359$ nT and $B_Y^{\mathrm{OFF}} = 5199$ nT, respectively.

[17] However, as shown in Figure 3 (bottom), the B_Z^{TAM} measurements lack symmetry along the horizontal Z axis in the ECI coordinates, and therefore we used the ±45° roll maneuver of the satellite body shown in Figure 4 to calculate the B_Z^{OFF}. Specifically, at time $t = t_1$,

$$B_Y(t = t_1 : +45^\circ) = B_Z(t - t_1 : -45^\circ), \quad (14)$$

and from equations (7) and (14), we can get

$$B_Y^{\mathrm{TAM}}(t = t_1 : +45) - B_Y^{\mathrm{OFF}} = B_Z^{\mathrm{TAM}}(t = t_1 : -45) - B_Z^{\mathrm{OFF}}, \quad (15)$$

so that by equation (14), we have finally

$$B_Z^{\mathrm{OFF}} = B_Y^{\mathrm{OFF}} - B_Y^{\mathrm{TAM}}(t = t_1 : +45) - B_Z^{\mathrm{TAM}}(t = t_1 : -45). \quad (16)$$

[18] *Lee et al.* [2001] calculated the generalized offset value for KOMPSAT-1 Z component, $B_Z^{\mathrm{OFF}} = -9000$ nT from equation (16) using telemetry data that we adapted for this study.

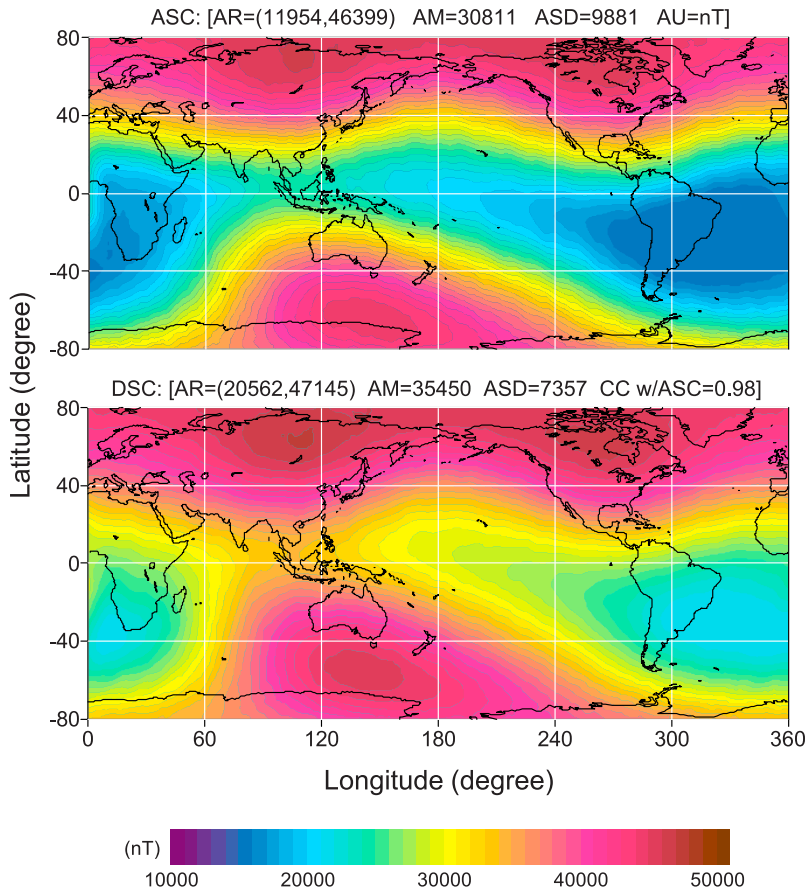

Figure 6. Total geomagnetic field estimates after removing the external field noise by wave number correlation filtering for the (top) ascending and (bottom) descending data sets.

[19] This simple approach may not entirely eliminate the induced fields by the spacecraft because the Earth's magnetic fields during the ascending B^A and descending B^D modes may change. This linear correction, however, considerably improves the similarity of the core field estimates between the ascending and descending data sets. After removing the self-induced and other noise, the gridded core field estimates now correlate at CC = 0.91 as shown in Figure 5. Thus this simple reduction has reduced the non-core field noise in the TAM estimates by about 50%. Further data processings from this point were performed in the spherical coordinates.

[20] To separate further the static internal field components from the time-varying external fields, we wave number correlation filtered the two maps in Figure 5 for their common internal magnetic field components. First, we geographically rearranged the given ascending (or descending) subparallel neighboring passes to isolate the spatially static features from the uncorrelated time-varying components and designed wave number correlation filters [*von Frese et al.*, 1997] from their correlation spectrum. The correlation spectrum gives the correlation coefficient (CC_k) between the two kth wave number components as the cosine of their phase difference $\Delta\theta_k$ (i.e., $CC_k = \cos(\Delta\theta_k)$). Figure 6 shows the core field estimates obtained from the wave number components that were passed only for $CC_k > 0$. The correlation filtered maps in Figure 6 now

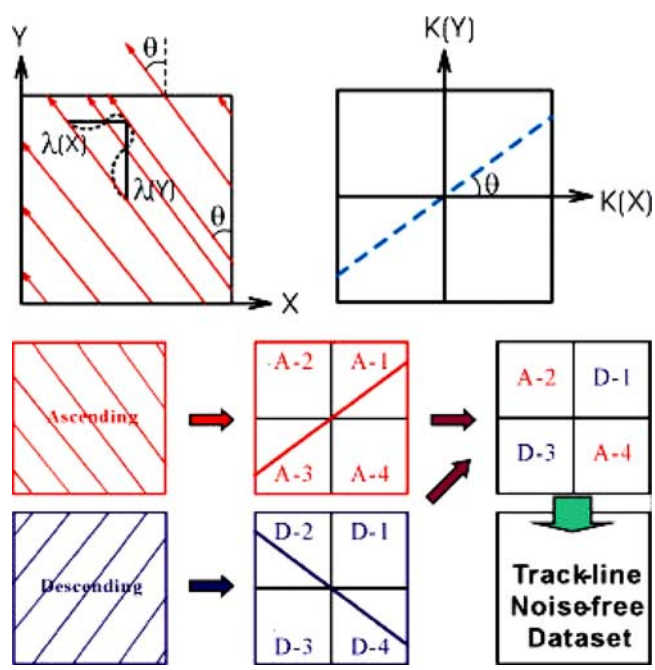

Figure 7. (top left) Track line noise geometries in the spatial domain and (top right) corresponding amplitude spectrum. Inverse transforming the noise-free quadrants A-2, A-4, D-1, and D-3 to the data domain produces estimates where the track line noise is reduced (lower).

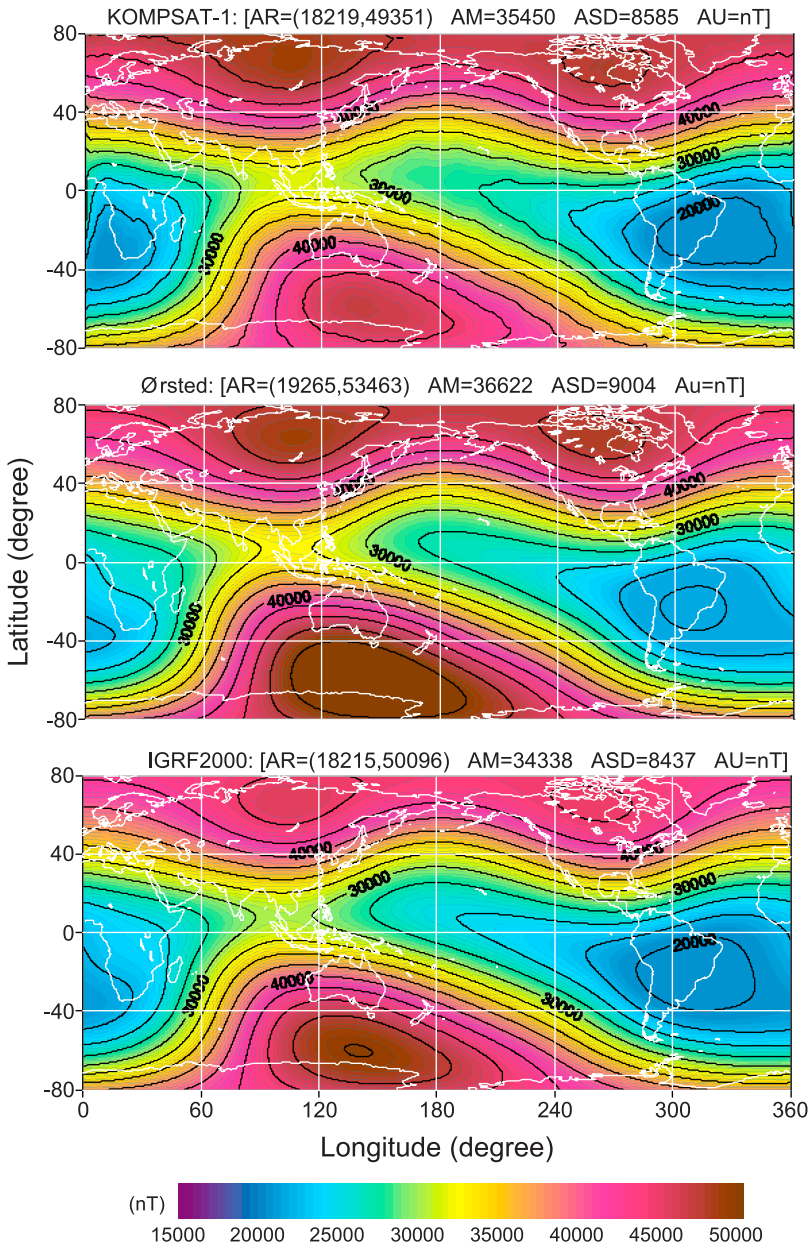

Figure 8. Total geomagnetic field components (F) from (top) KOMPSAT-1, (middle) Ørsted, and (bottom) IGRF2000 models.

correlate at CC = 0.98, which corresponds to a total reduction of about 77% in noncore field noise.

[21] Additional improvements in the core field estimates are possible by reducing the satellite track line noise in the maps of Figure 6. Spectral reconstruction can be used to help suppress these effects from filtering applied to the individual orbital data tracks [*Kim et al.*, 1998].

[22] For example, the line noise and KOMPSAT-1 track directions in Figure 7 (top) both subtend an angle of θ counterclockwise from the Y reference direction. The λ (X) and $\lambda(Y)$ wavelength components of track line noise in the X and Y directions, respectively, are related to θ by ($\tan\theta = \lambda(X)/\lambda(Y)$) Thus the spectral components of the noise occur in the quadrants that are orthogonal to the direction of the

Table 1. Statistical Comparison of Geomagnetic Fields From KOMPSAT-1, Ørsted, and IGRF2000 Models[a]

Mission	(Min, Max)	Mean	SD	Correlation Coefficient KOMPSAT-1	Ørsted	IGRF2000
KOMPSAT-1	(18,219, 49,351)	35,450	8,585	-	0.97	0.96
Ørsted	(19,265, 53,463)	36,622	9,004	0.97	-	0.99
IGRF2000	(18,215, 50,096)	34,338	8,437	0.96	0.99	-

[a]In units of nT.

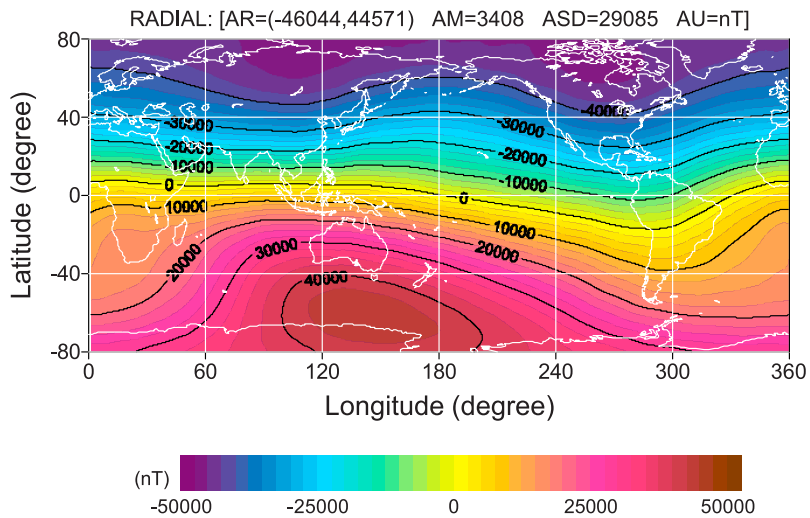

Figure 9. KOMPSAT-1 radial geomagnetic field components which were used to calculate the spherical harmonic coefficients.

lines, because the wave numbers, k, are inversely related to their wavelengths, λ, by ($k = 2\pi/\lambda$), so that ($\tan\theta = k(Y)/k(X)$) Accordingly, spectral distortions due to track line noise are limited only to the pair of symmetric quadrants shown in Figure 7 (top right), while the conjugate quadrant pairs are essentially uncontaminated [*Kim et al.*, 1998]. Hence, to construct the spectrum with minimum track line noise, we simply exchange the noise-contaminated quadrants in each of the data sets for the cleaner quadrants of the other data sets as shown in Figure 7 (bottom right) after normalizing the power level of ascending map to descending map by using mean values and the standard deviation. Inverse transforming the reconstructed spectrum gives the final core field estimates from the TAM measurements of KOMPSAT-1.

[23] Figure 8 shows total geomagnetic field components (F) from KOMPSAT-1 (upper), Ørsted (middle), and IGRF2000 models (lower), respectively. Table 1 compares the amplitude statistics between the three sets of gravity model estimates. The CCs between KOMPSAT-1 and the other two models are 0.97 and 0.96, and the (min, max), mean and the standard deviation values of the KOMPSAT-1 are between the two models.

3. Core Field Model Comparisons

[24] To develop a spherical harmonic model of the TAM core field estimates to compare with other core field models, we used the spherical harmonic series expansion up to degree and order of 10 for the potential ψ of the geomag-

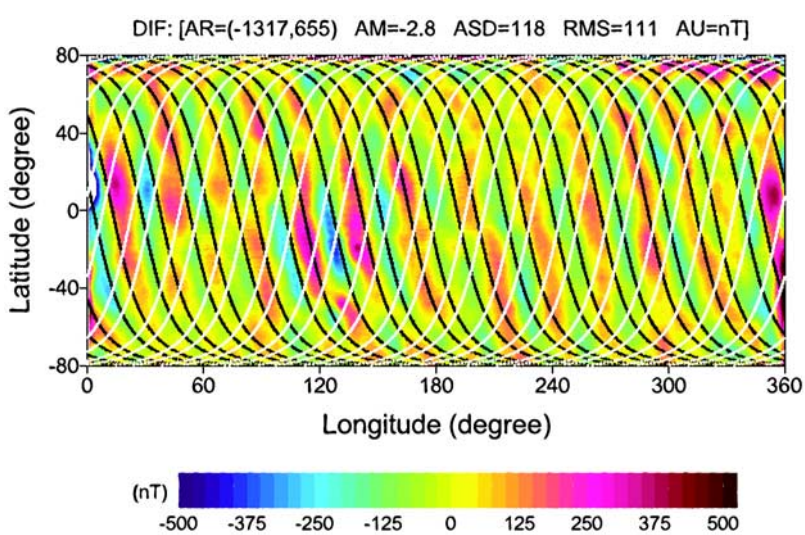

Figure 10. Differences between the gridded input to the spherical harmonic coefficient model up to 10 from KOMPSAT-1 measurements and calculated model, ranging from −1317 to 655 nT with the RMS value of 111 nT. White and black curves denote the ascending and descending ground tracks of the KOMPSAT-1, respectively.

Table 2. Spherical Harmonic Coefficients of the KOMPSAT-1, Ørsted, and IGRF2000 Geomagnetic Field Models up to Degree and Order up to 10

		KOMPSAT		Ørsted		IGRF2000	
n	m	g_n^m	h_n^m	g_n^m	h_n^m	g_n^m	h_n^m
1	0	−29570	0	−29617.37	0.00	−29615	0
1	1	−1829.2	5199.4	−1729.24	5185.65	−1728	5186
2	0	−2250.9	0	−2268.46	0.00	−2267	0
2	1	3126.6	−2370.9	3068.92	−2481.77	3072	−2478
2	2	1769.5	−311.74	1670.76	−457.62	1672	−458
3	0	1326.6	0	1340.16	0.00	1341	0
3	1	−2256.2	−295.23	−2288.34	−227.87	−2290	−227
3	2	1224.3	400.81	1252.09	293.28	1253	296
3	3	709.36	−442.14	714.08	−491.32	715	−492
4	0	903.81	0	932.11	0.00	935	0
4	1	767.08	276.13	786.66	273.21	787	272
4	2	259.94	−214.1	249.82	−231.70	251	−232
4	3	−390.97	99.748	−403.30	119.53	−405	119
4	4	136.19	−271.74	111.25	−303.65	110	−304
5	0	−211.8	0	−217.06	0.00	−217	0
5	1	334	53.062	351.98	42.76	351	44
5	2	184.43	183.24	222.06	171.19	222	172
5	3	−116.5	−141.2	−130.52	−132.88	−131	−134
5	4	−148.42	−47.613	−168.40	−39.42	−169	−40
5	5	−8.842	88.899	−12.92	106.44	−12	107
6	0	66.973	0	71.40	0.00	72	0
6	1	79.64	−19.948	67.40	−16.86	68	−17
6	2	76.686	55.337	74.17	64.34	74	64
6	3	−162.81	51.233	−160.81	65.34	−161	65
6	4	9.9755	−49.824	−5.77	−61.03	−5	−61
6	5	45.525	14.025	17.00	0.80	17	1
6	6	−74.346	63.417	−90.38	43.96	−91	44
7	0	75.653	0	79.07	0.00	79	0
7	1	−87.585	−64.312	−73.59	−65.03	−74	−65
7	2	−1.3731	−14.117	−0.04	−24.69	0	−24
7	3	38.124	5.3899	33.10	6.17	33	6
7	4	−0.54052	22.976	9.11	24.03	9	24
7	5	9.1284	15.324	7.03	14.87	7	15
7	6	4.143	−14.26	7.08	−25.34	8	−25
7	7	−0.93459	−12.80	−1.31	−5.71	−2	−6
8	0	20.134	0	23.92	0.00	25	0
8	1	13.481	7.51	5.99	12.18	6	12
8	2	−9.1907	−26.42	−9.20	−21.05	−9	−22
8	3	−5.6043	16.80	−7.74	8.63	−8	8
8	4	−11.871	−13.69	−16.54	−21.39	−17	−21
8	5	13.797	5.45	8.95	15.30	9	15
8	6	4.8978	16.89	7.03	8.76	7	9
8	7	0.65998	1.04	−7.97	−14.92	−8	−16
8	8	17.955	−0.14	−7.01	−2.46	−7	−3
9	0	11.931	0	5.30	0.00	5	0
9	1	−7.1483	−12.967	9.63	−19.91	9	−20
9	2	−5.5528	19.876	2.93	13.07	3	13
9	3	−12.001	9.7078	−8.58	12.50	−8	12
9	4	4.7004	3.3576	6.32	−6.23	6	−6
9	5	2.3069	−1.0151	−8.76	−8.31	−9	−8
9	6	−7.149	15.931	−1.53	8.46	−2	9
9	7	−2.9153	−6.8281	9.13	3.88	9	4
9	8	2.0165	0.16594	−4.24	−8.29	−4	−8
9	9	−4.8325	−3.8627	−8.09	4.88	−8	5
10	0	−10.098	0	−3.03	0.00	−2	0
10	1	17.731	−3.355	−6.46	1.87	−6	1
10	2	2.079	−6.5073	1.56	0.34	2	0
10	3	−6.8767	10.156	−2.95	4.12	−3	4
10	4	−5.4891	−3.0501	−0.32	4.94	0	5
10	5	19.589	−3.874	3.67	−5.86	4	−6
10	6	4.1235	3.9791	1.11	−1.18	1	−1
10	7	−2.1815	−3.4445	2.09	−2.84	2	−3
10	8	12.099	0.74861	4.41	0.24	4	0
10	9	10.188	−10.406	0.42	−1.98	0	−2
10	10	−5.5434	−22.373	−0.94	−7.67	−1	−8

netic field originating within the spherical Earth [*Langel and Hinze*, 1998] given by

$$\psi = a\sum_{n=1}^{\infty}\sum_{m=0}^{n}\left(\frac{a}{r}\right)^{n+1}\left[g_n^m\cos(m\phi) + h_n^m\sin(m\phi)\right]P_n^m(\cos\theta), \tag{17}$$

where a is the Earth's mean radius of 6371 km, (r, θ, φ) are the standard spherical Earth coordinates of the observations, P_n^m (cos θ) are the associated Legendre functions of degree n and order m, and g_n^m and h_n^m are the Gauss coefficients of the geomagnetic potential field within the Earth relative to P_n^m.

[25] To avoid errors due to additional corrections for θ and φ geomagnetic components, H^θ and H^φ, we used the radial (r) component of the KOMPSAT-1 measurements, H^r, to calculate the harmonic coefficients since r is always pointing to the center of the Earth. Figure 9 shows the KOMPSAT-1 radial geomagnetic field components which were used to calculate the spherical harmonic coefficient.

[26] Let P be the vector of spherical harmonic coefficients so that the matrix H of the spherical harmonic series becomes H^P and

$$c = H^p P + e, \tag{18}$$

where c is the column vector of N geomagnetic field observations and e is the error term [*Schmitz and Cain*, 1983]. For the radial component of the geomagnetic field, H^r, the ith row and jth column components, H_{ij}^r become

$$\begin{aligned} H_{ij}^r : (n+1)\cos(m\phi_i)P_n^m(\cos\theta_i)\left[\frac{a}{r_i}\right]^{n+2}\left(P_j = g_n^m\right) \\ (n+1)\sin(m\phi_i)P_n^m(\cos\theta_i)\left[\frac{a}{r_i}\right]^{n+2}\left(P_j = h_n^m\right), \end{aligned} \tag{19}$$

and we can calculate spherical harmonic coefficients by least squares using equation (19). Specifically, to avoid possible distortions caused by external field mainly in the horizontal components, we used the conjugate gradient method [*Hestenes and Stiefel*, 1952; *William et al.*, 1986] to relate KOMPSAT-1's geomagnetic field H_{ij}^r to the radial geomagnetic intensity B_z by

$$B_z = -H_{ij}^r P. \tag{20}$$

[27] We calculated the solutions which are the harmonic coefficients until the differences of the set of the solutions between consecutive estimates became less than 0.0001 nT.

[28] The differences between the gridded input to the spherical harmonic coefficient model up to degree and order10 from the KOMPSAT-1 measurements and calculated model in Figure 10 range from −1317 to 655 nT with

Table 3. Statistical Comparison of Input Data and Output Data[a]

Data	(Min, Max)	Mean	SD	CC
Input to model	(−43,715.12, 47,863.35)	−625.72	29,394.25	0.999
Output from model	(−43,560.64, 47,891.80)	−623.71	29,394.06	

[a]Input data (Figure 9) that were used to calculate the spherical harmonic model given in Table 2 and output data that were calculated from the harmonic model (through degree and order 10) in units of nT.

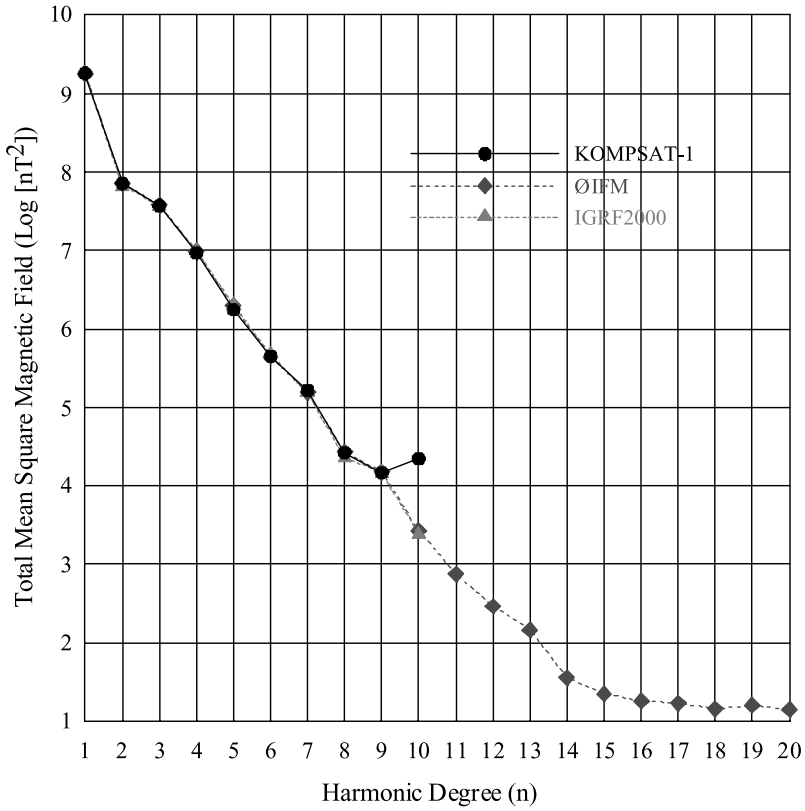

Figure 11. Radially averaged geomagnetic field spectra calculated from the KOMPSAT-1, ØIMF (Ørsted), and IGRF2000 models. The vertical axis values give the total mean square contribution to the magnetic field (nT^2) in log scale at the Earth's surface by the harmonics through degree n.

the RMS value of 111 nT. The errors in Figure 10 mainly reflect the limited measurement accuracy and orbital coverage of the KOMPSAT-1's TAM observations. Table 2 gives the spherical harmonic coefficients up to degree and order 10 from KOMPSAT-1's TAM data and also compares them with the Ørsted and IGRF2000 model coefficients. Table 3 gives a statistical comparison of input data (Figure 9) that were used to calculate the spherical harmonic model given in Table 2 and output data that were calculated from the harmonic model through degree and order 10. The CC between the input and out data files is nearly 1.0, and suggest that our spherical harmonic coefficients model is reliable. The output map is not shown since it is nearly identical to the map shown in Figure 9.

[29] Figure 11 compares the radially averaged power spectra, R_n, at the Earth's surface, calculated from

$$R_n = (n+1)\sum_{m=0}^{n}\left[\left(g_n^m\right)^2+\left(h_n^m\right)^2\right], \tag{21}$$

where g_n^m and h_n^m are the spherical harmonics coefficients when n and m are the orders and degrees for the KOMPSAT-1, ØIFM (Ørsted), and IGRF2000 models, respectively. The vertical axis values give the total mean square contribution to the magnetic field in nT^2 for the harmonic components through degree $n = 20$ for the ØIFM [*Olsen et al.*, 2000] model, and through degree $n = 10$ for the KOMPSAT-I and IGRF2000 models.

[30] The KOMPSAT-1 spherical harmonic core field model is well correlated with the other two models through degree $n = 9$. Thus the TAM observations significantly constrain important components of the Earth's core field despite their limited measurement accuracy.

4. Conclusions

[31] Our analysis of the TAM data from a limited number of KOMPSAT-1 orbits demonstrates their utility for mapping the Earth's core magnetic field components through degree and order 9. Even higher degree components may result from more extended TAM data sets coupled with more effective data selection criteria, but new investigations are required to quantify these issues. Thus despite their limited measurement sensitivity, the data records from satellite attitude control magnetometers offer new constraints for improved modeling of the satellite altitude behavior of the geomagnetic field since the late 1950s.

[32] **Acknowledgments.** The Korea Research Foundation supported this study under grant KRF-2001-041-D00259 and the Korea Aerospace Research Institute provided the KOMPSAT-1 data. Elements of this research were performed while J.W.K. held a National Research Council Senior Research Associateship Award at NASA Goddard Space Flight Center. J.S.H.'s research was supported by the National Research Lab Project (M1-0302-00-0063) of Korea Ministry of Science and Technology.

References

Alsdorf, D. E., R. R. B. von Frese, J. Arkani-Hamed, and H. C. Noltimier (1994), Separation of lithospheric, external, and core components of the south polar geomagnetic field at satellite altitudes, *J. Geophys. Res.*, *99*, 4655–4667.

Arkani-Hamed, J., and D. W. Strangway (1986), Magnetic susceptibility anomalies of the lithosphere beneath Europe and Middle East, *Geophysics*, *51*, 1711–1724.

Cain, J. C. (1966), Model of the Earth's magnetic field, in *Radiation Trapped in the Earth's Magnetic Field*, edited by B. M. McCormac, pp. 7–25, Springer, New York.

Campbell, W. H. (1997), *Introduction to Geomagnetic Fields*, Cambridge Univ. Press, New York.

Chapman, S., and J. Bartels (1940), *Geomagnetism*, Claredon, Oxford, U. K.

Chatfield, A. B. (1997), *Fundamentals of High Accuracy Inertial Navigation*, Am. Inst. of Aeronaut. and Astronaut., Inc., Reston, Va.

Foster, M. R., and J. Guinzy (1967), The coefficient of coherence, its estimation and use in geophysical data processing, *Geophysics*, *32*, 602–616.

Hestenes, M. R., and E. Stiefel (1952), Methods of conjugate gradients for solving linear systems, *J. Res. Nat. Bur. Stand.*, *49*, 409–436.

Jensen, D. C., and J. C. Cain (1962), An interim geomagnetic field, *J. Geophys. Res.*, *67*, 3568–3569.

Kelso, T. S. (1995), Orbital coordinate system, part I, *Satell. Times*, *2*(1), 80–81.

Kim, J.-H. (1996), Improved recovery of gravity anomalies from dense altimeter data, *Rep. 437*, 125 pp., Dep. of Geod. Sci. and Surv., Ohio State Univ., Columbus.

Kim, J. W., J.-H. Kim, R. R. B. von Frese, D. R. Roman, and K. C. Jezek (1998), Spectral attenuation of track-line noise, *Geophys. Res. Lett.*, *25*(2), 187–190.

Kim, J. W., H. R. Kim, R. R. B. von Frese, and C. H. Park (2003), Recovery of lithomagnetic components in the satellite magnetometer observations of east Asia, in *OIST 4 Proceedings, 4th Ørsted International Science Team Meeting*, edited by P. Stauning, pp. 99–106, Narayana, Odder, Denmark.

Langel, R. A., and W. J. Hinze (1998), *The Magnetic Field of the Earth's Lithosphere*, 429 pp., Cambridge Univ. Press, New York.

Lee, S.-H., S. W. Rhee, B. S. Suk, and K. L. Yong (2001), Measurement data analysis of three-axis-magnetometer in KOMPSAT-1, *J. Korean Soc. Aeronaut. Space Sci.*, *29*(3), 1–7.

Lee, S.-H., S. W. Rhee, and H. S. Ahn (2004), Slowly varying bias correction of magnetometer based on orbit geometry, *IEEE Trans. Aerosp. Electr. Syst.*, *40*(3), 1020–1030.

Maus, S., M. Rother, R. Holme, H. Lühr, N. Olsen, and V. Haak (2002), First scalar magnetic anomaly map from CHAMP satellite data indicates weak lithospheric field, *Geophys. Res. Lett.*, *29*(14), 1702, doi:10.1029/2001GL013685.

Neubert, T., M. Mandea, R. Hulot, R. von Frese, F. Primdahl, J. J. Ørgensen, E. Friis-Christensen, P. Stauning, N. Olsen, and T. Risbo (2001), High-precision geomagnetic field data from the Ørsted satellite, *Eos Trans. AGU*, *82*, 81, 87–88.

Olsen, N. (2002), A model of the geomagnetic field and its secular variation for epoch 2,000 estimated from Ørsted data, *Geophys. J. Int.*, *149*, 454–462.

Olsen, N., et al. (2000), Ørsted initial field model, *Geophys. Res. Lett.*, *27*(22), 3607–3610.

Schmitz, D. R., and J. C. Cain (1983), Geomagnetic spherical harmonic analyses: 1. Techniques, *J. Geophys. Res.*, *88*, 1222–1228.

Siouris, G. M. (1993), *Aerospace Avionics Systems: A Modern Synthesis*, Elsevier, New York.

UFO Investigator (1963), U.S. special project linked to UFOs, "Project Magnet Official," *11*(9), 1, June-Sept.

von Frese, R. R. B., M. B. Jones, J. W. Kim, and J.-H. Kim (1997), Analysis of anomaly correlations, *Geophysics*, *62*, 342–351.

William, H. P., B. P. Flannery, S. A. Teukolsky, and W. T. Vetterling (1986), *Numerical Recipes*, Cambridge Univ. Press, New York.

J. S. Hwang, Department of Earth System Sciences, Yonsei University, Seoul, 120-749, South Korea.

H. R. Kim, GEST/UMBC at Planetary Geodynamics Laboratory, NASA Goddard Space Flight Center, Greenbelt, MD 20771, USA.

J. W. Kim, Department of Geoinformation Engineering, Sejong University, Seoul, 143-747, South Korea. (jwkim@sejong.ac.kr)

S.-H. Lee, Satellite Control System Department, Korea Aerospace Research Institute, Daejeon, 305-333, South Korea.

R. R. B. von Frese, School of Earth Sciences, Ohio State University, Columbus, OH 43210, USA.